

Abstract

Charles Bridge in Prague is one of the most prominent historical structures in Europe. It was founded in 1357 by King Charles IV. The bridge interconnects two Prague districts, the Lesser Town and the Old Town, detached by the Vltava River. In the past, the bridge underwent a variety of damages, repairs and retrofits. Within the framework of the last reconstruction in 2007 - 2010, a measuring system was installed in the bridge and the temperature and moisture content at selected gauge points have been continuously monitored for a period of two years. This paper presents a non-linear coupled hygro-thermo-mechanical analysis of a current state after the last intervention. The analysis is based on Kiessl and Künzl's heat and moisture transfer model and a 3D orthotropic constitutive damage model. The main indicator of crack localization is the damage parameter. The cogency of temperature and moisture evolution is validated against experimentally obtained temperature fields.

Keywords: heat and moisture transfer, damage model, masonry arch bridge, finite element method.

1 Introduction

Charles Bridge in Prague belongs to the most prominent European historical structures (Figure 1 and 2). It is highly esteemed not only for its historical magnitude, but also for the economic contributions, caused namely by the attention of tourists.

The foundation stone was laid down on 9th July 1357 and the bridge itself was completed around 1406. This date and time were selected deliberately and had a ritual meaning numerically and astrologically (a numerical bridge: year 1357, 9.7., 5:31 AM). The King decided the Swabian builder Petr Parléř and his stone mason's workshop to manage the construction of the monument that ended in 1406. The quarter

towers today standing at the extremes of the bridge were both built later.

In the past, the bridge has suffered a lot of disastrous states, mostly due to floods and water erosion. Fortunately, after the last flood in August 2002, the bridge sustained without notable damage. The bridge also went through a variety of repairs and retrofits. The last two strongly influenced the actual structure. In the last century (1960s - 1970s), we witnessed its grouting, introduction of water-proofing layer, installation of stabilizing reinforced concrete slab, replacement of facing masonry and more recent actions. The last action, in July 2007 - June 2010, included the repair of parapets, hydroisolation of the pavement, and the rehabilitation of the foundations. It was based on a series of computational and experimental studies described in [1], [2], [3] and [4]. The complex underlying model was multi-scale due to the heterogeneity of the bridge on different levels, able to reflect non-linear material properties, multi physical and transient phenomena cover climatic effects as well as the interaction of the bridge with water and colliding vessels.



Figure 1: View of the bridge from South; St. Vitus Cathedral and the Castle on the background [5].

The analyses established that climatic loading should be considered most serious for the bridge as it is responsible for the nucleation and further development of cracks in the bridge. A suitable thermo-mechanical (or hygro-thermo-mechanical) analysis thus becomes the first thing when contemplating any actions such as, e.g., designing further stages of the bridge repair. In case of Charles Bridge, it is the retrofit of the bridge's sandstone cladding scheduled for the near future.

In this paper, the model presented is three-dimensional to take into account the voluminous proportion of the bridge. The simulation of coupled heat and moisture transfer in the stone masonry of Charles Bridge represents the first phase of the hygro-thermo-mechanical analysis and with the comparison of computer results with experimentally obtained data is thus the part of utmost importance. To keep the model complexity manageable, the second phase of the analysis - the prediction of damage evolution, is carried out in a staggered-coupled format. It means that transport phenomena serve as inputs for the mechanical part in each time step.

Such simulations of the evolution of temperature and moisture fields and their impact to the mechanical response are very arduous tasks and, especially, sequential computations of coupled problems are both time and memory consuming. Therefore, the parallelization of the problem based on the domain decomposition method was adopted. This method speeds up not only the solution of the system of algebraic equations, but also the evaluation of constitutive equations and assembling the system matrices. Details can be found in [6].



Figure 2: Charles Bridge in Prague (source: [12]).

2 Charles bridge

2.1 History and current state

Charles Bridge links both banks of the Vltava River, connecting the Old Town and the Lesser Town in Prague. It was the second arch masonry bridge in Prague, built to substitute the collapsed Judith's Bridge.

The bridge is 516.7 m long and 9.1 - 9.7 m wide, with 16 arches whose span varies from 16.6 to 23.4 m. It stands on 17 piers (each shielded by an ice guard) with cross section varying from 6.3 - 10.8 m by 24 - 25 m. Originally founded on millstones (either supported by oaken grillages or boxes anchored to the bed of the river), the piers have heads sharpened at an angle of 65° , to protect it against water stream and drifting ice. The subsoil is formed by a 5 - 10 m layer of coarse-grained gravel (with the particle size of up to 0.5 m) that lies on a rock massif consisting of Ordovic shales and quartzite [1]. The bridge is decorated with 31 statues in baroque style dating from

the beginning of the 18th century (many of them are copies, the originals can be seen in the Lapidarium of the National Museum). It had been lighted up by gas lighting since 1866, then it was adapted to electricity and (during the last restoration) to gas again [5]. The bridge has been for five centuries an important trade route but since 1966 it serves pedestrian only.

The bridge was damaged many times, mainly from floods and water erosion that caused periodic reconstruction, rehabilitation or strengthening, giving to the monument a great variability of materials and construction technologies in its different parts. The floods happened several times during the construction as well as after the completion with the last catastrophic event in 1890 which brought to the collapse 3 bridge spans (5th, 6th, and 7th vault). Due to the floods, the original foundations (millstones) were gradually replaced and some foundation of piers were rebuilt on a concrete caisson (see [1]).

2.1.1 Materials and structural elements

The bridge is mainly made up of Bohemian sandstone masonry. There are main three mesoscopic heterogeneity patterns distinguished in the body [1]:

- Regular periodic sandstone (upper Cretaceous quartz sandstone and carboniferous arkoses) ashlar (opus quadratum) facing of vaults (Figure 3 left), bound on lime mortar from sandstone stucco and hydraulic lime [7].
- Sandstone masonry (opus quadratum) with a non-periodic arrangement of blocks used in the facing of breast walls (Figure 3 in the middle).
- Filling irregular quarry masonry (opus caementicium) consisting of arenaceous marl blocks and mortar made of sand and black hydraulic lime (Figure 3 right). Classified as structural mortared rubble masonry (MRM technique) [3] according to the heterogeneous granulometry (from 5 to 50 cm) and the coarse particles. The aggregates are macroscopically very fine-grained (aleuropelitic) sedimentary rock of light beige to ochre colour. Despite the numerous interventions, the fill masonry is considered a Gothic original, since it is preserved in 13 out of 15 pillars and in 13 arches out of 16 [3].

Charles bridge is constructed as a classical masonry arch bridge, where massive piers support arches - vaults. An internal infill (Figure 4 part C), laterally covered by breast walls, makes the proper level for the flooring, that includes concrete slab, gravity concrete layers, today hydroisolation and granite paving. The breast walls (Figure 4 part B) stand on the bridge arches (Figure 4 part A); in the lower part, they are 0.9 m thick, while in the upper one, the thickness is 0.4 m. They were built without expansion joints and are reinforced at the connection with piers by masonry pillars that are also pedestals for statues (Figure 4). As the breast walls, also piers and vault arches



Figure 3: Periodic sandstone, non-periodic sandstone and filling masonry in the Charles bridge [5].

are built using bush-hammered blocks. The pier masonry is made up of granite blocks up to the level of the Vltva river, above it, the sandstone is used [7].

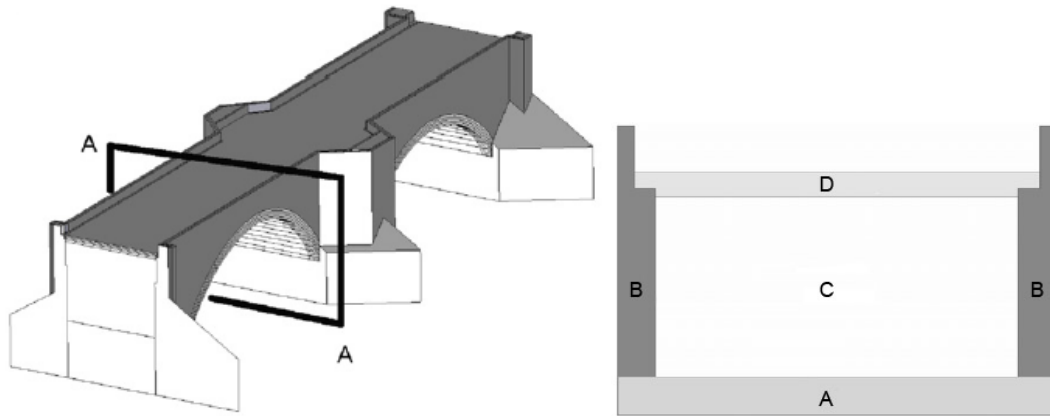


Figure 4: Schematic 3D view of Charles bridge with A-A section.

2.1.2 Last interventions

The present state of the bridge is mainly influenced by the last two reconstructions. In 1966 - 1975, the bridge was strengthened by high-pressure grouting and by a reinforce concrete slab (without expansion joints), covered by a bituminous waterproofing layer. There were also old stone blocks replaced. The passage to vehicles was excluded. It was later shown that some interventions during the reconstruction made very callous. This erroneous interventions of the 1960s-1970s brought problems with chemical, biochemical and physical degradation of the bridge. They also strongly influenced the interaction of bridge structural elements (e.g., body filler with the stone structure) and had a negative effect on the overall behaviour, contributing to the gradual mechanical disintegration of the structure. Most of mentioned problems are described in references [8], [4], [9] and [7].

A new intervention was performed in 2007 - 2010 to solve in a compatible way problems not only created by the 1960's - 1970's repair. It consisted in the rehabilitation of foundations as first step, followed by the hydroisolation of the pavement. Then repair of parapets, new navigation signs, and gas lighting to end of the work. In connection with the new hydroisolation and pavement layers, the existing concrete slab was cut and dilated in the middle and in the borders to create expansion joints and as such, to reduce the stresses related to its dilatation. Now, the expansion joint in contact with the breast wall is 150 mm thick and it is filled with gravel, while the one in the middle of the slab has thickness 20 cm and it is formed by extruded polystyrene [10].

To prevent cracks evolution in the parapets and breast walls caused by temperature changes, dilatation joints have been made in the stone railing masonry in correspondence with vault/pier intersection, and usually in every approx. 4 m. They are filled with a plastic mortar mixed with stone fragments (Figure 5). It was proven the parapets, as a part of the bridge, are the most affected by the up/down movements of the vault related to summer/winter changes and by the non-uniform temperature profile of the bridge body.

And finally, the most degraded stone blocks were replaced in parapets and breast walls. Despite all the efforts, the replacement was strongly criticized because the new stones do not match aesthetically the historical ones in their vicinity. All mentioned interventions are summarized in [5].

2.1.3 Current damage state and possible causes

As for mechanical degradation, there are visible cracks (thickness of millimetres) in vaults, breast walls and parapets. In the vaults the cracks are aligned and located approximately 1 m from the external face of the breast wall (Figure 6). They are present also in buttresses, near the pedestals for statues and in the corners between buttress and breast wall. Many minor cracks are present also in the monument but they do not represent a menace for the structural stability.

The recent studies explain the main causes of the crack development. It is assumed, thanks to previous repair, the damage is not related to movements of foundation [1]. The non-stress effects are considered causing the interaction of stone bridge structure, bridge body filler and breast walls prominently affecting the vertical deformations of the bridge vaults. The gradient of the non-uniform temperature changes of individual bridge parts (spatial distribution of temperature field) causes deformation and permanent strain. It leads to a gradual disintegration of the stone masonry, e.g., growing tilt of the breast walls [9], shear stresses development close to the external surfaces and in layers along the interface between sandstone masonry and irregular quarry masonry [1]. The shear stresses caused by differences in temperature are balanced by tensile stresses which cause the crack nucleation and development in the breast wall faces and vaults [11]. In the parapets, which have been recently repaired (2007 - 2010), cracks are expected to show again due to the periodic action of shear stresses related to the gradient of temperature between the upper and lower part of the parapet



Figure 5: Dilatation joint and contrast between old and new blocks [5].

and due to the vertical movements of the vaults (upwards in summer and downwards in winter). It is considered that, on the long period, the mechanism will bring to the ultimate damage the horizontal joints and consequently the repair of the parapet will be needed again. To reduce this effect, the above mentioned vertical joints filled with plastic deformable mortar have been added during the last repair (Figure 5).

3 Installation of measuring system and monitoring of temperature and moisture fields

During the last intervention a measuring system was installed to monitor and record the temperature and moisture content. The continuous monitoring of temperature and moisture fields requires that a sufficiently dense network of reliable sensors be provided. To this end, four cross-sections of the bridge were selected and are plotted, together with the logger's position, in Figure 7 for illustration.

The control system has been allocated under the twelfth vault on the Lesser Town's side of the bridge. Cross-sections 1 and 2 situated in arch XI are 36 m and 34 m away from the logger's position, respectively. The distance of cross-sections 3 and 4 (arch VIII) from the logger is 128 m and 137 m, respectively. Several gauge points are located in the selected cross-sections 1 through 4 (C.S. 1 - 11pts., C.S. 2 - 13 pts., C.S. 3 - 11 pts., C.S. 4 - 15 pts.). Each measuring point has been fitted with three temperature sensors and with one moisture sensor. To cope with demanding simulations just one segment of the bridge, one half of arch VIII, was examined in computer experiments. The corresponding set-up in cross-sections 3 and 4 is displayed

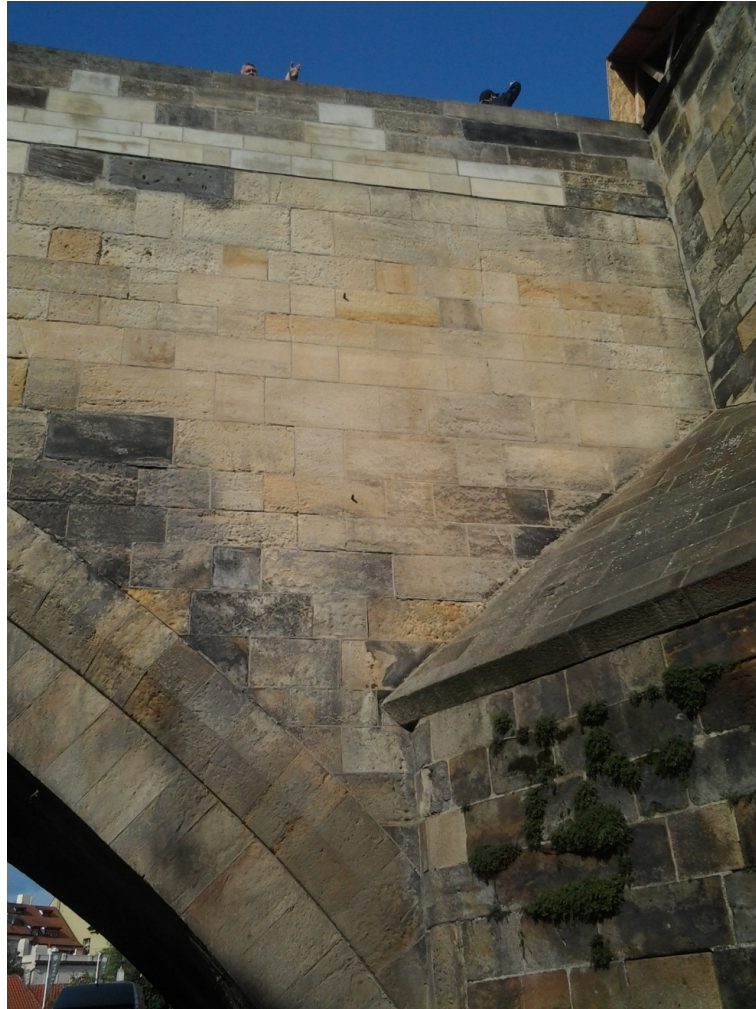


Figure 6: Visible vertical cracks in the southern breast wall of arch No. XI near pillar No. 10.

in Figures 9 and 8.

The accessibility of the sensors in the future (say within next fifteen years) will be impossible. To enhance the reliability of the measuring system the temperature sensors have been implemented in triplets. Such an arrangement makes it possible to detect a prospective defect applying the method of selection (two correct solutions of three). Just one sensor of moisture has been installed at each point because of its price. The gauge points are denoted with a triplet of figures and characters. Thus, 3D1 indicates cross-section 3, borehole D, and gauge point 1. The sensors are denoted correspondingly. It means that BT 3D1:1, BT 3D1:2, and BT 3D1:3 stand subsequently for temperature sensors 1, 2, and 3, respectively, while the moisture sensor situated at the same point is denoted as BH 3D1:4. Selected data are stored under this notation in the Information System, see [12].

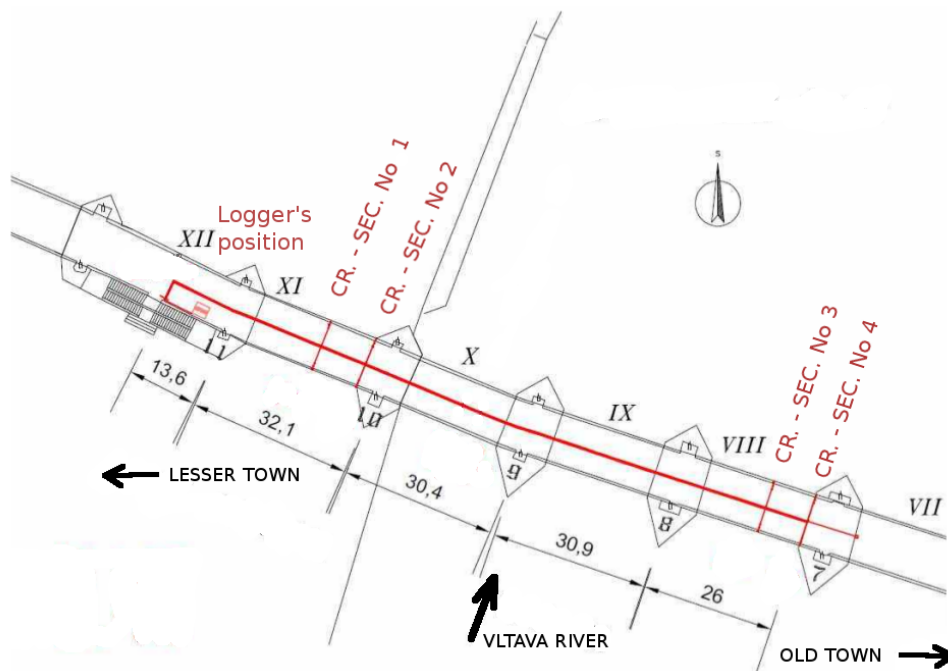


Figure 7: Layout of cross-sections selected for sensors instalment.

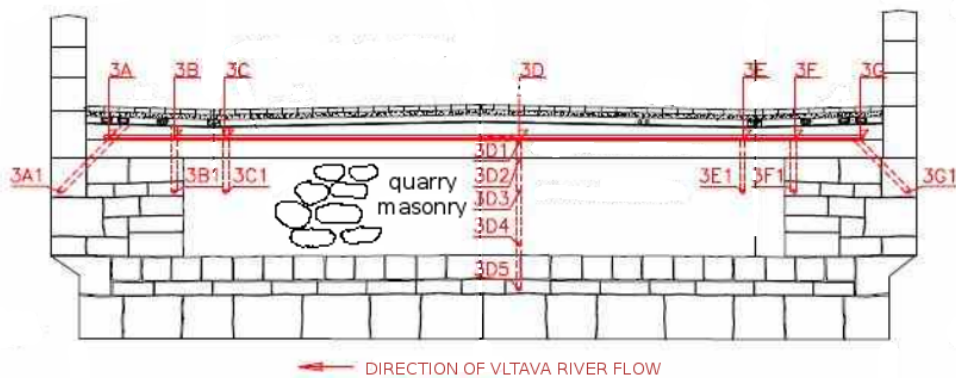


Figure 8: Cross-section 3 - gauge points (11 points, i.e. 33 temperature sensors and 11 moisture sensors).

Temperature measuring was performed by the Pt1000 thermometers, imbedded in a special resin in a stainless casing, 6 mm in diameter. Four strand shielded conductors were delivered with no interconnections because of the system's reliability. The sensors were subjected to accelerated ageing in a climatic chamber (cycling between 30 - 100°C and with samples submerged in warm acid, alkali and water). Moisture sensors were also imbedded in special porous ceramics and connected with an electric resistivity-voltage transducer made to order. Calibrating was provided by means of the gravimetric method exploiting samples extracted from the test pit.

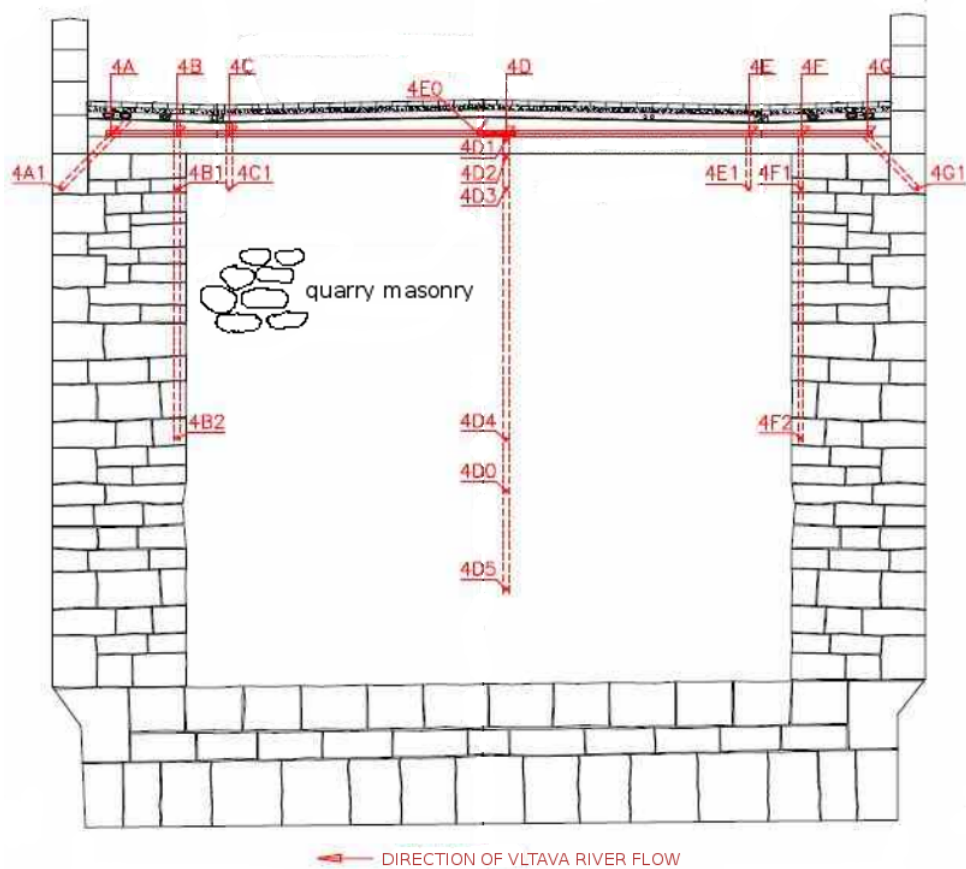


Figure 9: Cross-section 4 - gauge points (15 points, i.e. 45 temperature sensors and 15 moisture sensors).

4 Numerical model

4.1 Description of heat transfer and numerical solution

Comparing the computationally and experimentally obtained results would seem preposterous if the model's properties were not comprehensively specified. The presented numerical simulations are based on Künzle and Kiessl model [13]. Advantage of such an approach is its simple application to the analysis of building structures in normal climatic conditions and easy and quick applying of physical material properties obtained from laboratory measurements. This very popular model is briefly summarized in the following section.

Two unknown variables are introduced at each material point, the relative humidity φ [-] and the temperature T [K]. The over-hygroscopic region is split into two parts - the capillary water region and the supersaturated region with different conditions for liquid water and vapour transport. The relative humidity is considered the only

moisture potential for both the hygroscopic and over-hygroscopic region. It is encouraging that despite taking on certain simplifications the model covers all substantial phenomena and predicts the results which can be validated by measurements (see Section 4.4). Three sets of equations enter the solution procedure, namely constitutive equations (retention curves, material properties), transport equations (Fick's law, Darcys law and Fourier's law) and continuity equations. A more detailed description can be found, e.g., in [6]. The governing equations - the heat and moisture balance equations, are closely coupled because the moisture content depends on the total enthalpy and thermal conductivity while the temperature depends on the moisture flow. The resulting equations for the description of the heat and moisture transfer are expressed in terms of the temperature T and the relative humidity φ and assume this form

$$\frac{\partial w}{\partial \varphi} \frac{\partial \varphi}{\partial t} = \nabla^T (D_\varphi \nabla \varphi + \delta_p \nabla (\varphi p_{\text{sat}})), \quad \mathbf{x} \in \Omega, \quad (1)$$

$$\left(\rho C + \frac{\partial H_w}{\partial T} \right) \frac{\partial T}{\partial t} = \nabla^T (\lambda \nabla T) + h_v \nabla^T (\delta_p \nabla (\varphi p_{\text{sat}})), \quad \mathbf{x} \in \Omega, \quad (2)$$

where λ [$\text{W m}^{-1} \text{K}^{-1}$] is the thermal conductivity of the moist material. H_w [J m^{-3}] denotes the enthalpy of the material moisture, w [kg m^{-3}] is the water content of the material, h_v [J kg^{-1}] is the evaporation enthalpy of the water, p_{sat} [Pa] is the water vapour saturation pressure, ρ [kg m^{-3}] is the material density, C [$\text{J kg}^{-1} \text{K}^{-1}$] is the specific heat capacity and t [s] denotes time. The liquid conductivity D_φ [kg m s^{-1}] is the product of the liquid diffusivity D_w [$\text{m}^2 \text{s}^{-1}$] and the derivative of water retention function $D_\varphi = D_w \cdot dw/d\varphi$. The vapour diffusion resistance number μ is a material property and δ [$\text{kg m s}^{-1} \text{Pa}^{-1}$] is the vapour diffusion coefficient in the air.

The finite element method is called for the spatial discretization and the weighted residual statement is applied to the mass balance equation (1) and energy conservation equation (2), which lead to the final system of differential equations specified in a compact form:

$$\mathbf{C}(\mathbf{d})\dot{\mathbf{d}} + \mathbf{K}(\mathbf{d})\mathbf{d} = \mathbf{f}, \quad (3)$$

where the dependency of the conductivity \mathbf{K} and capacity \mathbf{C} matrices on the attained values of variables is explicitly denoted. Letters \mathbf{d} and $\dot{\mathbf{d}}$ denote increments of nodal variables and their time derivatives. The system of equations (3) is then solved incrementally using the Newton-Raphson method for non-linear system of algebraic equations, see e.g., [14] or [15] to mention a few references.

4.2 Damage models

4.2.1 Orthotropic damage model

The stone masonry similarly as concrete can be classified as a quasi-brittle material which has a relatively high ratio of compressive strength to tensile strength. The

progressive loss of its material integrity due to the propagation of microcracks, microvoids and other similar effects can be well described by damage models. More details about the model can be found in [16] and [17]. Generally, the damage models consist in concepts of virgin, damaged and pseudo-undamaged states of material. The material is assumed to be at virgin state when no defects are present which corresponds to the elastic state.

One of the simplest models of continuum damage mechanics is the scalar isotropic damage model with a single scalar parameter. The main drawback of the scalar isotropic damage model is that it uses only one damage parameter for all principle directions regardless of tension or compression [18], [19]. Once the damage parameter evolves due to exceeding limit strain in one principle direction, it reduces stiffness in all remaining principle directions even though they should not be influenced. This drawback is not significant in the case of one-dimensional stress state such as pure bending but it becomes more important especially for a three-dimensional stress state with the combination of temperature loading. In this case, anisotropic damage model or orthotropic damage model can be more accurate. As for anisotropic damage model, laboratory measurements of required material parameters have to be performed but it causes difficulties for certain cases. Additionally, the model requires a significant number of internal variables that have to be stored. These difficulties led to the development of a simplified version of the model which relies on six material parameters - three for tension and another three parameters for compression. It means that orthotropic damage model introduces a symmetric second-order damage tensor instead of one damage parameter. The tensor is uniquely described by three principal values corresponding to principal directions [21].

The model is based on the following stress-strain relation

$$\sigma_\alpha = (1 - H(\hat{\varepsilon}_\alpha)D_\alpha^t - H(-\hat{\varepsilon}_\alpha)D_\alpha^c) \left[\left(K - \frac{2}{3}G \right) \hat{\varepsilon}_{vol} + 2G\hat{\varepsilon}_\alpha \right], \quad (4)$$

where $\hat{\varepsilon}_\alpha$ is the principal value of the strain tensor with the index α of the principal component. H denotes the Heaviside function, K is the bulk modulus, G is the shear modulus and $\hat{\varepsilon}_{vol}$ is the total volumetric strain. The model defines two sets of damage parameters D_α^t and D_α^c for tension and compression, respectively.

There are many evolution laws that can be used for D_α^t and D_α^c description. For our problem, the two evolution laws for the damage parameters are used similar to the laws used in the scalar isotropic damage model. The first law gives better results for compression but the determination of the material parameters is more complicated. The second law involves correction of the dissipated energy with respect to the size of elements and it describes tension better. It is defined by the non-linear Equation (5) which can be solved using the Newton method

$$(1 - D_\alpha^\beta) E |\hat{\varepsilon}_\alpha^\beta| = f_\beta \exp \left(-\frac{w^\beta}{w_{cr0}^\beta} \right). \quad (5)$$

In the above equation, f_β represents the tensile or compressive strength, w_{cr0}^β controls

the initial slope of the softening branches, E is Young's modulus, h is the characteristic finite element length and $w^\beta = D_\alpha^\beta h |\hat{\varepsilon}_\alpha^\beta|$ and stands for the crack opening width [m].

4.3 Computational model

The numerical model simulates the coupled heat and moisture transfer and mechanical response of one half of arch III in the course of two years, 2011 - 2012. The finite element mesh was created using tetrahedron elements with linear approximation functions. It has 73749 nodes and 387773 elements (Figure 10).

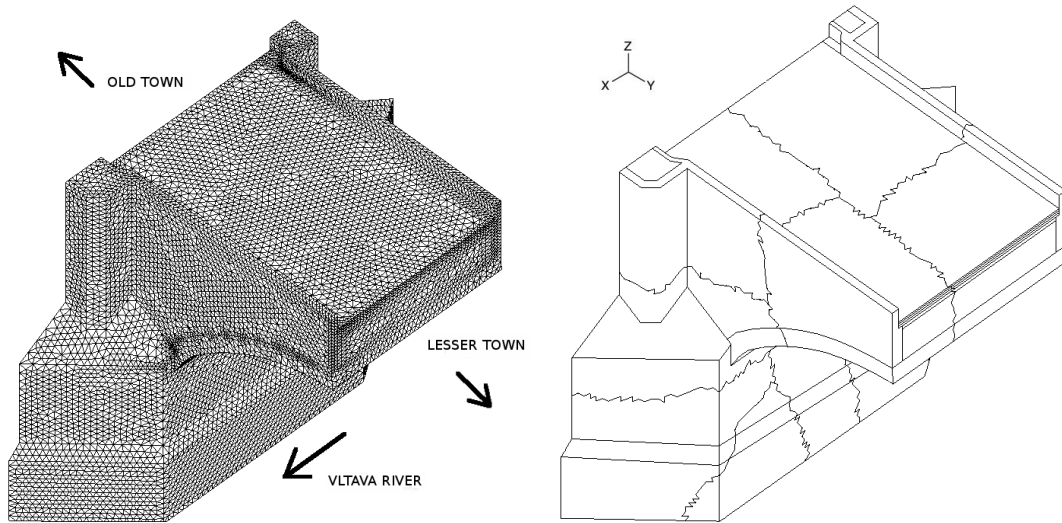


Figure 10: 3D finite element mesh model of one half of the arch III (left) and its domain decomposition (right).

With regard to computer memory requirements, the parallelization of the problem based on the domain decomposition method was inevitable. Domain decomposition methods split the original domain solved into several smaller sub-domains which are assigned to processors of a parallel computer (a cluster of computers). A parallel version of the SIFEL computer code was used [21] with the distributed memory scheme and the MPI communication library, which uses the master and slaves concept where the master processor manages communication among all processors and it also controls the computation. The Schur complement method was applied due to a non-linear and non-symmetric final system of equations (3). The method was built on the factorization and the nonlinear system was solved by the modified Newton-Raphson method, which uses the initial Jacobi matrix, and the factorization of the matrix was performed only once in each time step. The analyzed segment taken out of Charles Bridge was split into 12 sub-domains. The average number of nodes and elements on one sub-domain is 7000 and 32000, respectively. Parallel computation was performed on a heterogeneous PC cluster where computers are based on the 32 bit Intel E6850 processors with a different frequency in the range of 2.4 to 3 GHz and the memory

from 3GB to 3.3 GB. The parallel algorithm performed 7596 time steps. A time step was set to cover two hours (7200 seconds). The overall consumption of the computation (CPU) time was one month.

The staggered algorithm was chosen for the hygro-thermo-mechanical analysis, where data (temperature and moisture fields) are transferred from the transport part to the mechanical one. For the mechanical analysis, the finite element model corresponds to the current state after the last reconstruction in 2007 - 2010. The mesh is divided in several different element and material groups, e.g., pier masonry, infill of the pier, vault, infill of the vault, northern breast wall, southern breast wall, concrete slab, first layer upon the concrete slab, second layer upon the concrete slab, pavement, with dilatation and expansion joints (plastic mortar and extruded polystyrene).

4.4 Validation of simulations against monitoring

The first step of the hygro-thermo-mechanical analysis was the verification and validation of heat and moisture transfer model and its material parameters. The boundary conditions for this part of the analysis were specified with respect to representative climatic data, see [20], including the effect of sun radiation, wind, rain, heat conditions, and the structure's orientation. Subsequently, after estimating the extreme surface temperatures of the annual cycle at -15°C and 52°C for the winter and summer season, respectively, a three-dimensional temperature field was analyzed solving linear steady-state heat transfer problems implementing homogenized material parameters and the surface and interior temperatures obtained from two-dimensional data. The 3D non-stationary evolution of temperature and moisture fields in Charles Bridge was analyzed in conjunction with its last repair [11] and [5], when a measuring system was installed in the bridge and the temperature and moisture content at selected gauge points have been continuously monitored for a period of two years. The only simplification applies to the moisture field. As evident from the monitoring, see Figure 11, the moisture content evolves only insignificantly within the scrutinized period.

Taking this fact into consideration, the additional fully coupled heat and moisture transfer approach was carried out in a shorter period to assess a three-dimensional distribution of the moisture field which was then considered to remain stationary, as the difference between the evolution of the moisture content predicted on the one hand by simulation and on the other by monitoring seems to be inessential. It was experimentally ascertained that the percentage increase of the moisture content varies from 5 to 12%, see selected curves in Figure 11. These curves confirm the assumption of nearly stationary moisture content at individual material points (it varies in space, but hardly in time). Some of the sensors are adversely affected by disturbances coming from the environment (e.g., induced voltage), see end parts of the graphs in Figure 11 (lower). In any case, the reliability of the temperature sensors is much higher in comparison to the sensors monitoring the moisture content.

This finding allowed us to account for the dependence of the heat transport parameters on the moisture content and assume the temperature as the only problem

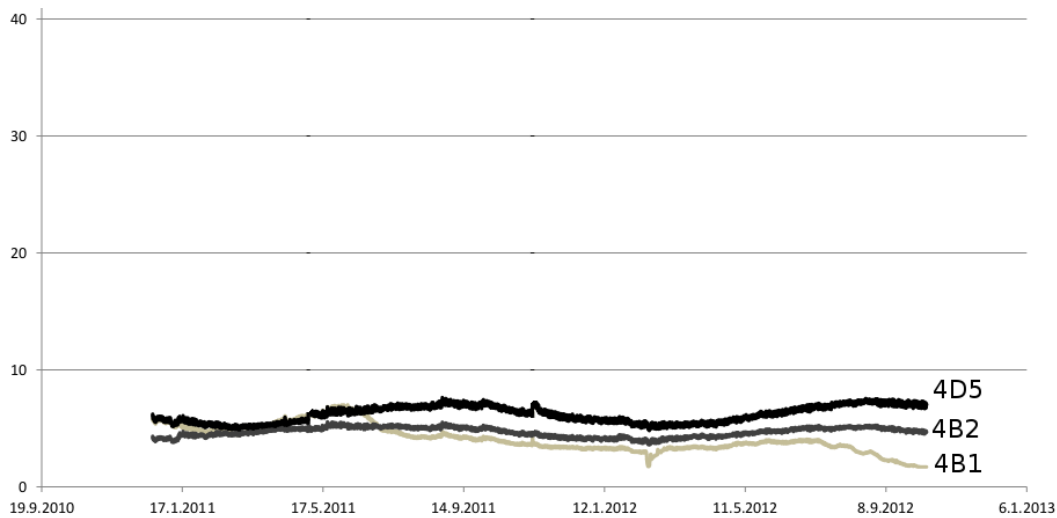


Figure 11: Measurement of the percentage increase of moisture content at gauge points 4D5, 4B2, 4B1 [%].

unknown. The boundary and initial conditions were formulated in the same way as in the above described simplified approach. Two hours were set for the integration step, so that twelve values a day were simulated to cover local fluctuations. In order to spare printing time just one value of a daily set was collected and displayed in graphs. This, moreover, facilitates discerning the simulated temperature courses from the monitored data (delivered every ten minutes, i.e. 144 values a day).

The selected comparison of evolutions of the monitored and computed temperatures at individual gauge points are shown in Figures 12 and 13. In the early period of the calculation, a noticeable disproportion, typical of all points, is apparent between the simulated and monitored data. This is due to the incorrectly predicted distribution of the initial temperature field. Fortunately, this spurious phenomenon vanishes soon afterwards, say within 3 months at the most, and does not devalue the relevant results.

Going through these figures in detail, two findings draw attention. First, the temperature maxima in summer on the southern surface are higher by roughly 7 - 8°C compared with the northern surface. This estimate was corroborated by independent measurements at 48 points on the vertical surfaces of Charles Bridge and at 9 points located at the lower surface of arch X. To this end, the COLTCRAFT IR 650 12D temperature gauge was successfully utilized. This effect, attributed to solar radiation, is prominent namely at interior points 3A1 and 3G1, the corresponding difference of the temperature maxima interval being about 4°C. The second finding shows a certain shift between the simulated and monitored data in time, which becomes more perceptible at the points approaching the surface of the vault. As was discovered by a direct measurement of surface temperature, such an undesirable discrepancy was brought about by improperly specified boundary condition on the lower surface of arch VIII. Apparently, the exterior temperature was influenced not only by the shielding against

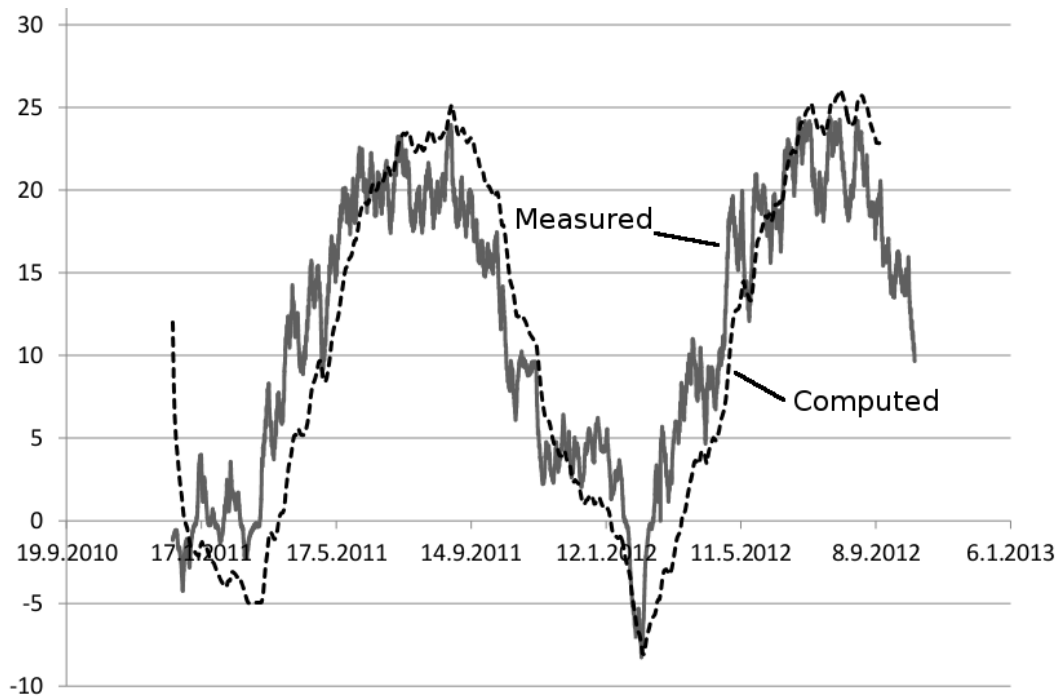


Figure 12: Distribution of temperature at gauge points 3A1 [degree centigrade]

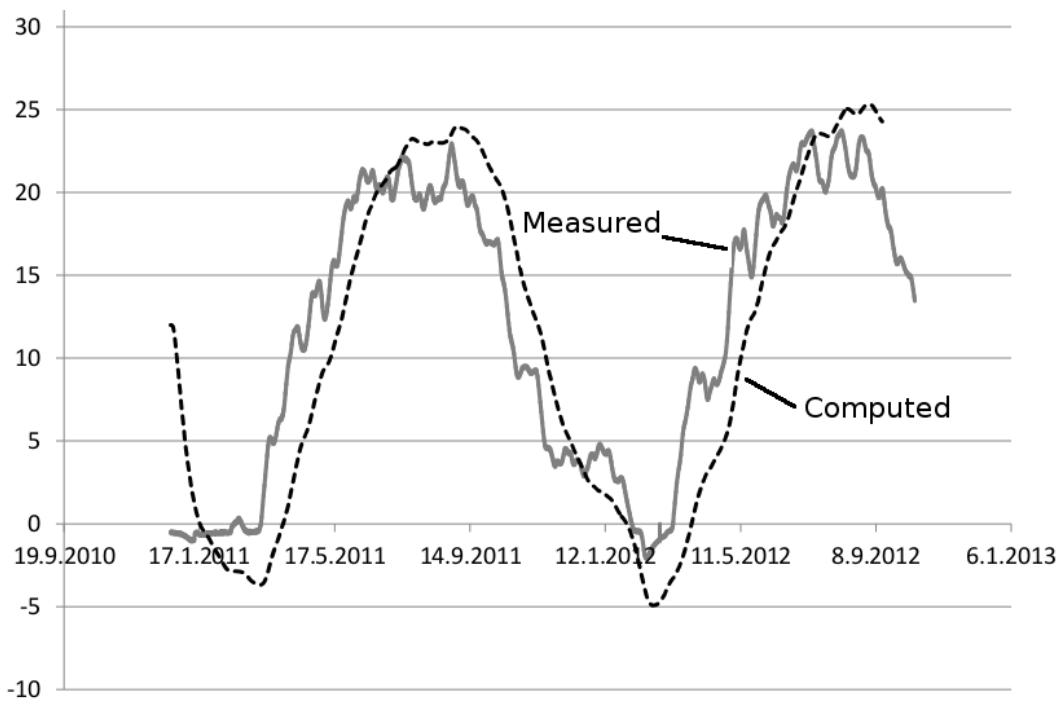


Figure 13: Distribution of temperature at gauge points 3B1 [degree centigrade]

solar radiation, but also by the temperature of water running under the bridge, which should be accounted for as well. Another reason for the lag between the simulated and monitored data could be attributed to the imperfect homogenized transport parameters of a strongly heterogeneous material.

It is also interesting that the daily fluctuations become stronger with a decreasing distance from the bridge's surface whereas they are smoother in the internal regions of the bridge. The temperature of water affects the surface temperature of the bridge foundations. In this case study, the water table was considered steady and equal to the average year level [11].

4.5 Results of computation and prediction of the bridge behaviour

Owing to the fact that moisture content is not varying significantly during the annual cycle, the thermo-mechanical analysis is then performed with the staggered algorithm. The computation covers the period from April 2011 to October 2012. The boundary conditions and the homogenized material parameters for the heat transport are taken over from the previous coupled heat and moisture transfer problem validated against in situ measurements. The initial temperature field was set just on April 2011 as the average values for the oscillating annual temperatures. Due to the computational time and memory and CPU requirements, the time step was set to two hours (7200 seconds) for the heat transport part and to one week (604800 seconds) for the mechanical analysis, respectively.

Apart from the temperature loading entering the mechanical part of the analysis, two mechanical loadings were added to the FE model. The first one is the self weight. The second one is the pedestrian live load of 5 kN/m^2 on the pavement prescribed according to Eurocodes. Material parameters entering the mechanical computation were chosen from references [11] and [5].

The mechanical response of the structure is demonstrated by the deformed shape with the displacements, the stress state, the damage parameters (in three principal directions) and the corresponding crack opening width. The bridge arch moving during a one year cycle, upwards in summer and downwards in winter, is regarded as a bridge breathing. The maximum vertical displacement is about +3 mm and -2 mm in summer and winter, respectively. Due to the non-uniform temperature distribution and differences between southern and northern surface temperatures, the arch also twists and bends in horizontal direction. The maximum horizontal displacement is approximately 1.5 mm. Moreover, both parapets along with the upper parts of breast walls twist and deflect from the vertical plane. The displacements of parapets in horizontal direction reach 1 mm.

The maximum values of compression stress remain in elastic range, while the tensile stress reaches its limit value in the regions, where damage develops. The damage parameter and mainly the corresponding crack opening width provide basic information about possible damage evolution in the bridge. The damage parameters in two principal directions (in tension) are approaching one in the most stressed parts of the

bridge, while in the third principal direction (in compression) it equals to zero. The first principal direction coincides with the horizontal axis y of the bridge axis (see Figure 10) and the second principal direction corresponds to the horizontal axis x perpendicular to the longitudinal bridge axis.

Figure 14 illustrates the distribution of damage parameters in the body of arch III. There are distinct damage zones in the quarry masonry filling and in the transition zone between the filling and the sandstone masonry of the breast walls. These distributions are underpinned with the spatial distributions of the temperature field in cross-sections 3 and 4 plotted in Figures 15 and 16, respectively. They show the regions where damage might be anticipated. Namely, the strong temperature gradients, accentuated in these figures with a sudden variation of colours, give rise to shear stresses in the proximity of the surfaces of the bridge and, consequently, originate massive damage in the layers localized along the interface between the quarry and sandstone masonry. The shear stresses are balanced out by tensile stresses, which then initiate the nucleation and further development of cracks in the vault and on the breast wall faces.

Figures 17 and 18 show damage parameters distributions and Figures 19 and 20 display the corresponding crack opening width. There are three main distinct zones of possible damage evolution in parapets and breast walls. The first zone is situated near the connection of the breast wall and pillar (Figure 19). This zone is characterized by the tensile stress due to the bridge bending. The second damage zone (Figure 20) is in the middle part of the breast wall under the bed joints of the parapet. This sort of damage is probably caused by shear stresses arising due to the differences in temperature field. The third zone is in the breast wall in the lower part of pillar (Figure 20) and is probably brought about also by the tensile and shear stresses resulting from the differences in temperature. Even the differences in temperature in the mere vertical direction and in the cross-section of the bridge arch give rise to the deformation of parapets and breast walls working against the adjacent bridge body. This effect then provokes the tensile and shear stresses evolution. The maximum crack opening width in the first principal direction reaches $1.0 \cdot 10^{-1}$ mm and the maximum crack opening width in the second principal direction is about $1.5 \cdot 10^{-2}$ mm. There is one extra visible damage zone (Figure 19) in concrete layers under the pavement, which is caused mainly by the differences in temperature in conjunction with the different thermal dilatation coefficient of materials.

The very important finding is that the damage in the vault appears only in perpendicular (horizontal) direction, not in the direction of the bridge and vault axis, and its crack opening width reaches a maximum value of $1.0 \cdot 10^{-3}$ mm. This is why the vault is almost undamaged.

It should be pointed out that a one year cycle analysis was subsequently extended by further annual cycles to explore the effect of cyclic temperature loading and to obtain a prediction of the bridge behaviour in the near future. The slight progress of displacements, the evolution of existing damage zones, and the development of new small damage zones during the second year of simulation (an increase is about 10%) were discovered when analyzing the results. This state of the bridge has remained

unchanged since.

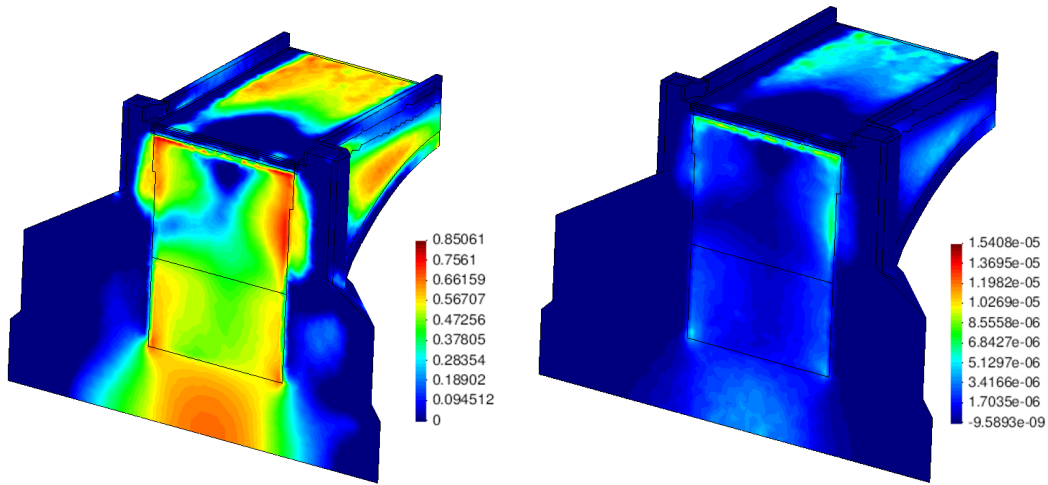


Figure 14: Spatial distribution of damage parameter in the bridge structure in summer time after one year cycle in the first principal direction (left) and corresponding width of cracks openings (right).

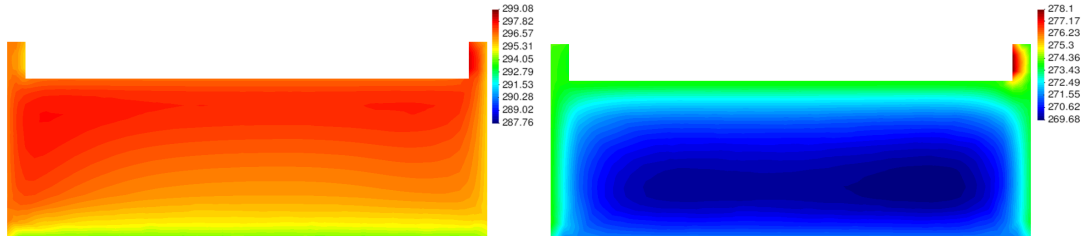


Figure 15: Spatial distribution of temperature [Kelvins] in cross-section 3 in summer (left) and in winter (right)..

Bolstered by this analysis we are justified to claim that the structure is currently stable and safe and that the thermal loading has the utmost impact on the bridge's behaviour. Precisely, decreasing temperatures toward winter provokes the highest tensile stress state and therefore the biggest damage. As already underlined in [1], considering the temperature cycle it can be noticed that this loading is not a threat for the stability of the structure (according to the used model, the maximum displacement (deflection) is about 3 mm).

The results imply the tendency of the structure to damage in agreement with the real crack distribution observed on site, mainly on arches 5, 6, 10, 11 and 12 where the damage state is higher than in arch 3 (the one used in the model because of its known geometry).

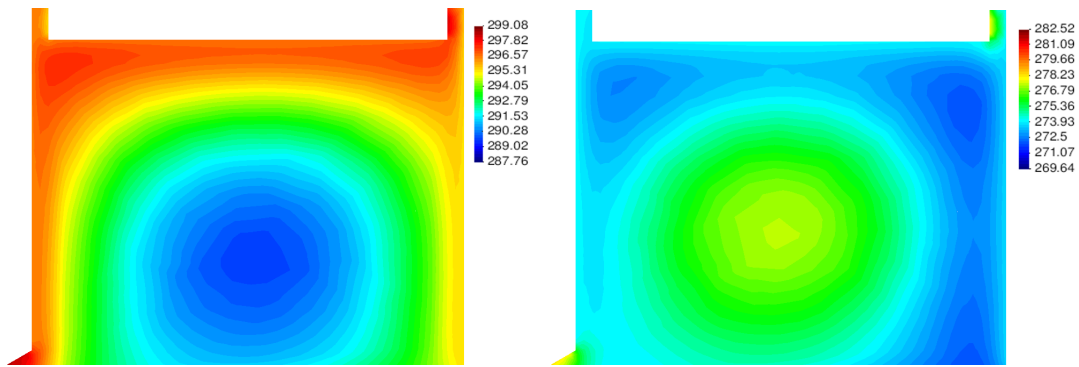


Figure 16: Spatial distribution of temperature [Kelvins] in cross-section 4 in summer (left) and in winter (right).

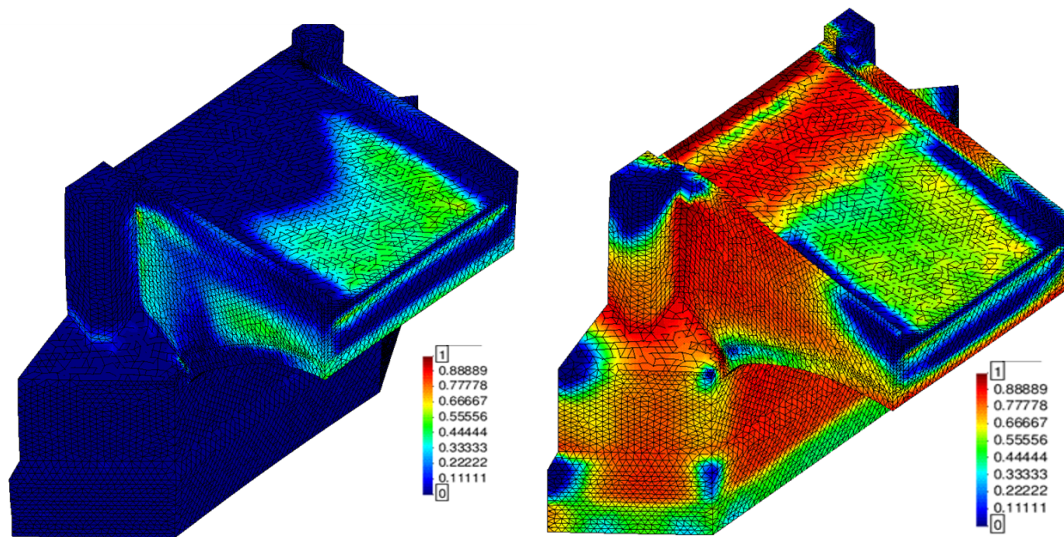


Figure 17: Deformed shape and damage parameter after two year cycles in the first principal direction in summer 2011 (left); in winter 2012 (right).

The last rehabilitation deserves to be commented in the light of FE model. The release of the connection between the breast walls and concrete slab undoubtedly prevents the breasts from damage. The vertical dilatation joints (filled with plastic mortar) spare the damage on parapets, though they cannot prevent the propagating cracks into breast walls underneath the joints. The conclusion is that the damage related to thermal loading in the bulky structure cannot be avoided. It is possible to change its distribution, trying to move it from the weakest structural parts or just from the eye (as achieved with the last intervention). On the other hand, the low maximum crack width computed for the actual bridge configuration implies that the problem is mainly aesthetic and only the repetition of cycles with exceptional temperatures, combined with the presence of low quality blocks or mortar, can subsequently lead to clearly visible

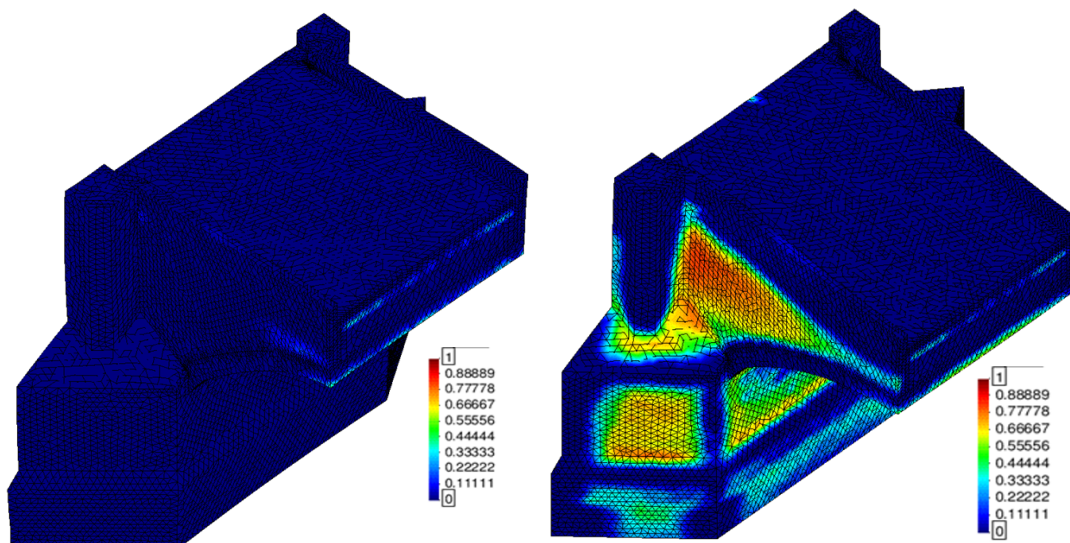


Figure 18: Deformed shape and damage parameter after two year cycles in the second principal direction in summer 2011 (left); in winter 2012 (right).

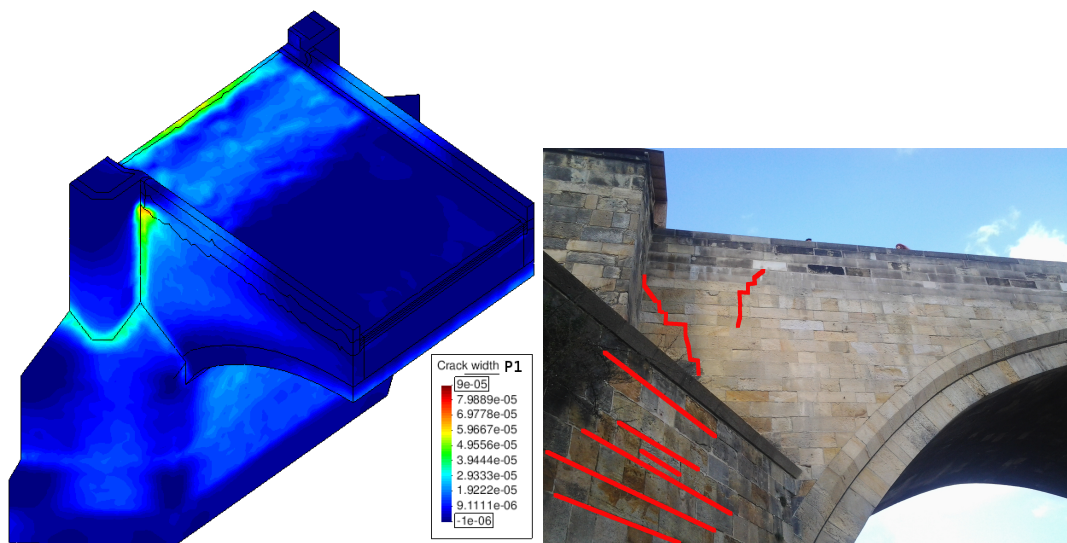


Figure 19: Distribution of the width of crack openings computed from tensile damage tensor after two year cycles in the first principal direction (left) in winter 2012; red highlighted visible cracks in breast walls (right) of arch X.

damage. A final aspect to notice is that the initial condition of the FE model (absence of damage) slightly deviates from reality, as some small cracks were still visible even after rehabilitation and replacement of blocks, therefore the reliability of the model cannot be admitted without reservations.

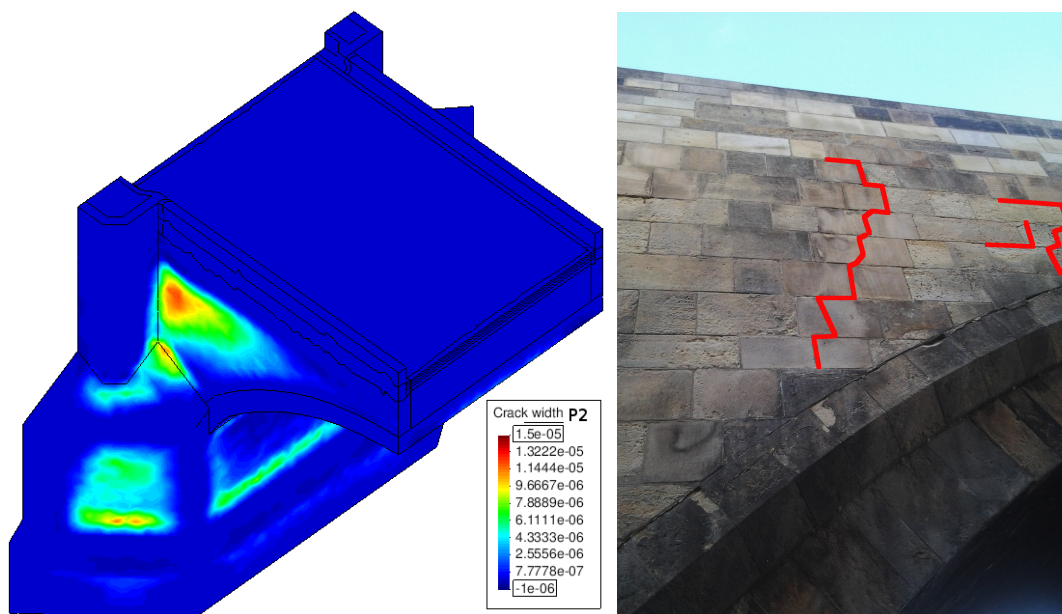


Figure 20: Distribution of the width of crack openings computed from tensile damage tensor after two year cycles in the second principal direction (left) in winter 2012; red highlighted visible cracks in breast walls (right) of arch X.

5 Conclusions

This paper has two aims. The first aim is to demonstrate a reliable approach to the description of a coupled heat and moisture transport in voluminous stone masonry structures, such as Charles Bridge in Prague, using computer simulations. To this end, the well-tried material (constitutive) model by Künzle and Kiessl was addressed in conjunction with the SEPUC homogenization strategy [22]. The paper presents the evolution of both temperature and moisture fields obtained by a continuous monitoring of these quantities at selected gauge points in the bridge. Eventually, the results of computer simulations were validated against those obtained experimentally. A detailed investigation of computed results manifests a lag of heat transfer at internal points in comparison with the ones in the vicinity of the bridge surface. Whereas this phenomenon is thermodynamically correct, a slight discrepancy between the computational prediction and the measurement is, in the first place, ascribed to an imperfect prior estimate of transport parameters. It can be deduced that the thermal conductivities of individual phases (and subsequently of masonry as a whole) were undervalued, while the phase heat capacities could likely be overvalued. Decreasing the daily fluctuations of temperature, while passing inside the bridge, is another thermodynamically unobjectionable phenomenon. On the other hand, the smoothed out simulated courses correspond to taking only one value a day when drawing individual courses. As for the moisture content, it is worth noting that this quantity varies rather slowly in the course of time. This finding is somewhat disappointing after the expensive hydroisolation of

the bridge deck has been implemented. Nevertheless, the moisture content appears to be plausible.

The second aim of this paper is to obtain a notion about the current mechanical state of Charles Bridge. The results presented in this paper will serve as a serious basis for providing a reliable estimate of real states of stress and damage in Charles Bridge. As has already been mentioned, climatic loading is the most serious one for stone bridges as it is responsible for the nucleation and further development of cracks. The 3D simulations using the SIFEL computer code implicate two causes of periodic damage in the parapets: shear stresses due to the temperature differences between the upper and lower parts of the parapets (roughly 2 - 3°C) and the vertical movements of the vaults (upwards in summer and downwards in winter) - the breathing of the bridge. There is no doubt that after a certain period of time both reiterating mechanisms will lead to the ultimate damage in the horizontal joint and the need not only for maintenance but for an all-out repair of the parapets. On the other hand, the damage state and cracks evolution do not influence distinctly the stability and bearing capacity of the bridge.

Acknowledgements

Financial support for this work was provided by GAČR project No. 15-17615S. The financial support is gratefully acknowledged.

References

- [1] J. Zeman, J. Novák, M. Šejnoha and J. Šejnoha, Pragmatic multi-scale and multi-physics analysis of Charles Bridge in Prague. *Engineering Structures*, 30(11), 3365-3376, 2008.
- [2] A. Št'astná, R. Příkryl, J. Jehlička, Methodology of analytical study for provenance determination of marbles. *Journal of Cultural Heritage*, 10, 82-93, 2009.
- [3] R. Příkryl, A. Št'astná, Contribution of clayey-calcareous silicite to the mechanical properties of structural mortared rubble masonry of medieval Charles Bridge in Prague (Czech Republic), *Engineering Geology*, 115, 257-267, 2010.
- [4] R. Příkryl, Z. Weishauptová, M. Novotná, J. Příkrylová, A. Št'astná, Physical and mechanical properties of the repaired sandstone ashlar in the facing masonry of Charles Bridge in Prague (Czech Republic) and an analytical study for the causes of its rapid decay, *Environmental Earth Sciences*, 63(7-8), 1623-1639, 2011.
- [5] M. Toesca, Thermo-Mechanical Analysis of Charles Bridge. Faculty of Civil Engineering, Czech Technical University in Prague, Master thesis, 2014.
- [6] T. Koudelka, T. Krejčí, J. Kruis, Modeling of Building constructions in SIFEL Environment. Czech Technical University in Prague: CTU Reports, 2011.
- [7] J. Witzany, T. Cejka, R. Zigler. Failure Resistance of Historic Stone Bridge Structure of Charles Bridge. II: Susceptibility to Floods, *Journal of Performance of Constructed Facilities*, Marc/April, 22(2), 83-91, 2008.

- [8] Z. Bergman, Charles Bridge Museum. (<http://www.charlesbridgemuseum.com/>), 2009.
- [9] J. Witzany, R. Zigler. The analysis of non-stress effects on historical stone bridge structures (monitoring, theoretical analysis, maintenance), *Journal of Civil engineering and Management*, 13(2), 157-167, 2007.
- [10] Mott MacDonald, Partial report on Charles Bridge, Prague, 2011.
- [11] T. Krejčí, J. Šejnoha, Evolution of temperature and moisture fields in Charles Bridge in Prague, Computational prediction and measurements. *International Journal of Architectural Heritage*, in print.
- [12] Karlův most IS. (<http://iskarluvmost.fsv.cvut.cz/>), 2010.
- [13] Künzel H. M., Kiessl K. Calculation of heat and moisture transfer in exposed building components, *Int. J. Heat and Mass Transfer*, 40, 159-167, 1997.
- [14] Z. Bittnar and J. Šejnoha, *Numerical Methods in Structural Mechanics*, ASCE Press, New York, USA, 1996.
- [15] M. A. Crisfield, *Non-linear Finite Element Analysis of Solids and Structures*, John Wiley & Sons Ltd, Chichester, UK, 1991.
- [16] J. Lemaitre, J. L. Chaboche, *Mechanics of solid materials*, Cambridge University Press, Cambridge, UK, 1994.
- [17] J. Skrzypek, A. Ganczarski, *Modeling of Material Damage and Failure of Structures*, Springer-Verlag Berlin Heidelberg, Germany, 1999.
- [18] E. Papa, A. Taliervo, Anisotropic Damage Model for the Multiaxial Static and Fatigue Behaviour of Plain Concrete, *Eng. Fract. Mech.*, 55(2), 163-179, 1996.
- [19] J. Mazars, G. Pijaudier-Cabot, Continuum damage theory - application to concrete, *J. Eng. Mech-ASCE*, 115, 345-365, 1989.
- [20] K. Ďurana, J. Maděra, R. Černý, R. Database of climatic data as a rewarding tool for inclusion of weather observations in computational service life assessments of historical buildings, *WIT Transactions on the Built Environment*, 131, 245-256. 2013.
- [21] J. Kruis, T. Koudelka, T. Krejčí, Multi-physics Analyses of Selected Civil Engineering Concrete Structures. *Commun. Comput. Phys.*, 12, 885-918, 2012.
- [22] J. Sýkora, J. Vorel, T. Krejčí, M. Šejnoha and J. Šejnoha, Analysis of coupled heat and moisture transfer in masonry structures, *Materials and Structures*, 42 (8), 1153-1167, 2009.